Satellite Detected Around a Star's Substellar Companion

Kevin Hoy[1,2,3*], Alice Zurlo[1,3], Pablo A. Peña R.[1,4], Jana Köhler[5], Silvano Desidera[7], Raffaele Gratton[7], Cecilia Lazzoni[7,3], Simon Petrus[6,3], Florian Rodler[2], Jonathan Smoker[2], Valentina D'Orazi[8,9], Ilaria Carleo[7], Ilaria Giovannini[10,1,7,3]

[1]Instituto de Estudios Astrofísicos, Facultad de Ingeniería y Ciencias, Universidad Diego Portales, Av. Ejército Libertador 441, Santiago, Chile.
[2]European Southern Observatory, Alonso de Córdova 3107, Casilla 19, Santiago 19001, Chile.
[3]Millennium Nucleus on Young Exoplanets and their Moons (YEMS).
[4]Centro de Astrofísica y Tecnologías Afines (CATA), Casilla 36-D, Santiago, Chile.
[5]TLS Tautenburg, Sternwarte 5, 07778 Tautenburg, Germany.
[6]NASA-Goddard Space Flight Center, Greenbelt, MD 20771, USA.
[7]INAF-Osservatorio Astronomico di Padova, Vicolo Osservatorio 5, 35122 Padova, Italy.
[8]Dept. of Physics, University of Rome Tor Vergata, via della Ricerca Scientifica 1, 00133 Rome, Italy.
[9]INAF Osservatorio Astronomico di Roma, via Frascati 33, Monte Porzio Catone, 00040 Rome, Italy.
[10]Dipartimento di Fisica e Astronomia, Università degli Studi di Padova, Vicolo dell'Osservatorio 3, 35122 Padova, Italy.

*Corresponding author(s). E-mail(s): kevin.hoy@mail.udp.cl;

Abstract

Despite more than 6000 exoplanets being discovered to date[1], no satellite orbiting an exoplanet, an *exomoon*, has ever been confidently detected. While there are some candidates, they lack clear and convincing confirmation and remain controversial[2–5]. Beyond the innate

value of discovering new types of objects in the Universe, satellites can help give key insights into formation mechanisms and the dynamical evolution histories of their systems. In this work, we present evidence for the existence of a satellite orbiting the directly-imaged brown dwarf companion CD-35 2722 B. We have applied radial velocity analysis, the same technique used to discover the first exoplanet around a Solar-type star[6], on spectra of this brown dwarf obtained with VLT/CRIRES$^+$. We have found what appears to be the periodic signal induced by at least one orbiting satellite. This is the first time this technique has successfully produced evidence of satellites around a companion brown dwarf. Our best-fitting model includes a satellite candidate with a minimum mass of ∼0.7 Jupiter masses and an orbital period of ∼170 days. While it is uncertain if this satellite fulfills the presently-undefined criteria to qualify as an exomoon, it is a significant step towards that first detection, as advancing technology will allow the same method to be applied to less massive targets.

1 Main

CD-35 2722 B (hereafter CD-35 B for brevity) is a young brown dwarf (BD) discovered via direct imaging in 2011[7]. At a projected separation of ∼2.8", it is well-resolved from its host star. It's orbit was partially constrained in a future study, finding that it has a high eccentricity (>0.9) and a long period of ∼5000 years, although many parameters are poorly constrained due to the short coverage of its wide orbit[8]. It is a 37 M_{Jup} companion to a 0.4 $M_\odot$ M-type star, making the mass ratio between host and companion relatively low for this system[7,9]. It has been calculated that, in the event of satellites orbiting CD-35 B, the radial velocity method would be relatively likely to find them[10].

We conducted a VLT/CRIRES$^+$[11] program (PI: Zurlo, 0112.C-2053(A), 0114.C-2039(A) **& PI: Hoy, 116.2AP9**) to monitor the radial velocity (RV) variation of the target induced by possible satellites from October 2023 through **February 2026**. Given the projected separation of CD-35 B and the narrow 0.2" slit of CRIRES$^+$, we were able to obtain the spectra of the companion itself, without significant contamination of the primary star. **We obtained 26 epochs in total, but one is discarded in this analysis due to a very low signal, while two more are rejected for poor weather (these latter observations were quickly redone in better conditions), thus we are left with 23 high-quality observations.** Each epoch is an AB nodding sequence, giving us the ability to subtract sky contamination while also taking two separate spectra each night. The data were reduced using the official ESO pipeline recipes[1].

The method employed in this work was first suggested in 2018[12]. It has been attempted in the past, targeting other directly-imaged substellar companions with different instruments. GQ Lup B[13] and HR 7672

[1] https://www.eso.org/sci/software/pipelines/cr2res/cr2res-pipe-recipes.html

B[14] were observed with KPIC, a high-resolution spectrograph (R≈35,000) built for characterizing directly-imaged planets. The HR 8799 planets were observed with Keck/OSIRIS, a medium-resolution integral-field spectrograph (R≈4000)[15]. None of those companions showed RV variation at each work's respective precisions. Compared to those works, we are able to achieve RV results one to two orders of magnitude more precise. These previous works employed a forward modeling approach in order to properly account for stellar contamination in the brown dwarf/planetary spectra. This method has known challenges for RV extraction, including disparate result when fitting different orders[16]. Our data, lacking stellar contamination, allows us to avoid the use of theoretical models. See Section 2.1 of Methods for a more detailed discussion of contamination characterization. The higher resolution of our data (R≈100,000), should also provide some precision improvement, although this difference is likely small compared to the difference in methodology.

Objects orbiting such high-mass substellar companions, having not been discovered before, have some ambiguity regarding their taxonomy. For this work, we will use the term "satellite" to refer to the body/bodies we are presenting. This is meant as a neutral term simply meaning "an object orbiting a significantly larger object", in the same sense that the Moon is a satellite of Earth, and the Earth is a satellite of the Sun. More discussion on this question of classification is included at the end of the article.

To extract the RVs of CD-35 B, we used `viper`[17,18], a template-matching RV code with built-in CRIRES$^+$support. This code creates an empirical template combining every spectrum to maximize its signal-to-noise ratio. The individual spectra can then be compared to this template to measure their relative RV over time. We run `viper` for all 46 (23 nights, 2 nodding positions per night) spectra of CD-35 B, then bin the RVs of the nodding pairs to maximize precision (more details in Methods). The extracted RVs are shown in Fig. 1.

As an initial check for periodicity in our RVs, we created a Generalized Lomb-Scargle (GLS) periodogram[19]. This is a function that measures how likely it is that a data set is periodic at a given period. GLS periodograms often produce false peaks aliased from artifacts in the data, and so to determine the validity of a peak, there are defined False Alarm Probability (FAP) thresholds that can be calculated based on the number of observations and their relative time sampling[20]. In our data, there is a peak near a 170-day periodicity that crosses the 0.1% FAP threshold, denoting a high degree of confidence that there is some periodic signal in the data. The GLS periodogram for our data is shown in the first panel of Fig. 2.

Beyond observing a strong periodicity in our data, we use the `EMPEROR` code[?] for Keplerian fitting of the RV data. The best-fitting models are presented in Fig. 1. We are able to fit our data with different models invoking different numbers of satellites. `EMPEROR` iterates through these models until the current iteration fails to meet a fit-quality criterion, at which point the previous is accepted as the best-fitting model. **To check for time-dependent noise (and rotational effects, to be discussed later), we applied Gaussian Processes (GPs), but ultimately found that**

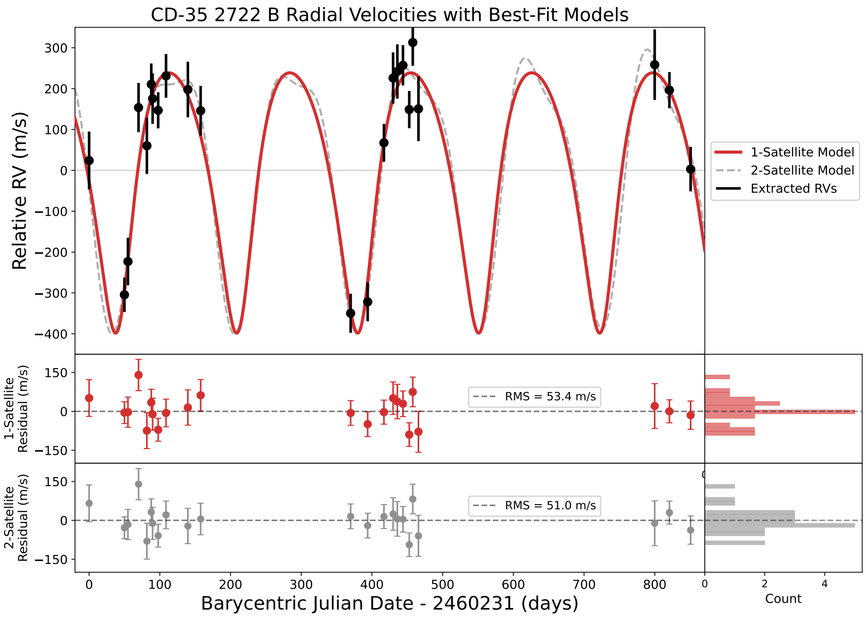

Fig. 1 Extracted relative RVs for CD-35 2722 B with best-fitting one-satellite and two-satellite models. All BJD, RV, and RV error values are available in Appendix A, with the full corner plot for the favored model in Appendix B.

we do not recover any extra signals. We therefore assume an independent gaussian noise model for this work, in order to avoid over-modeling the noise. It is likely that, due to a combination of factors, our systematic errors are significantly higher than any real jitter caused by unconstrained physics, and thus this noise model is the most applicable. Section 2.3 of Methods contains details on this analysis.

There are two models which are almost equally capable of explaining the data. One is a one-satellite model, with a period of ∼170 days, an $\mathrm{msin}\, i$ **of** ~ 0.9 $\mathrm{M_{Jup}}$**and an eccentricity of ∼0.27. The other model involves a similar satellite, but on a circular orbit, with an accompanying inner satellite. There is some degeneracy for the parameters of this inner satellite, hence the multiple peaks in panel C of Fig. 2. The most likely model, though, gives a period of ∼86 days, very near a 2:1 mean-motion-resonance (MMR). The best-fitting model parameters are shown in Table 1.**

These two models are very similar, due to the known degeneracy between single eccentric orbits and MMR orbits[21]. From simulations, it is common for 2:1 MMR orbits to mimic eccentricities near 0.3, the same as the best-fitting one-satellite model[22]. This means that, from RV data alone, it is presently very difficult to distinguish between the two models. The derived periods are slightly different from such an exact resonance, so over time the models should diverge.

As a test to help confirm the detection(s) of the satellite(s), we used N-body simulations with `REBOUND` to test the stability of the models[23,24]. The one-satellite model is generally stable over long timespans, even in what we expect to be its most unstable configuration. The two-satellite model, however, is highly unstable. Even internally, ignoring any perturbation from the central star, the BD-satellites system is so chaotic that for most configurations, one of the satellites is ejected within 500 years, a small fraction of the BD's orbit. The only stable configurations are when the two satellites are within 20° of coplanar orbits, and they have counter-rotating orbits. While there are some questions surrounding formation for both models, which must be addressed in future work, this need to produce counter-rotating, circular, 2:1 MMR orbits seems significantly more difficult than the challenges facing the formation of the single eccentric satellite (many of which are shared with the two satellite model as well). A more detailed exploration of system stability is present in section 2.4 of Methods.

Therefore, while both models are strictly possible, and cannot be distinguished between by our RV data, we find it more likely that the one-satellite model is accurate due to these stability considerations. Further discussion will thus center on this model.

Unfortunately, we cannot make any assumption about the inclination of the orbit of the satellite and therefore, estimate its true mass. In the Solar System, while all the planets orbit within the ecliptic, their moons do not. Rather, regular satellites (which includes all of the most massive moons in the Solar System except Neptune's Triton) orbit in the plane of their hosts' equator, and the obliquity of CD-35 B is entirely unconstrained. The extreme eccentricity of the BD's orbit also makes assuming orbit-rotation axis alignment more dubious, as it suggests a more complex dynamical history. However, it is quite unlikely that the satellite is a second brown dwarf, as the inclination correlated with a true mass of 13 M_{Jup}, the generally-accepted lower limit for brown dwarfs, is only $\sim 4°$, very close to a face-on orbit.

This eccentric single-satellite model is a contextually interesting result for the system, as a high satellite eccentricity would align with the host's very high eccentricity of >0.9[8]. As the host-satellite pair follows its own highly eccentric orbit, the variation in gravitational force from the host star could cause an increase in the eccentricity of the satellite. For exoplanets in S-type orbits in stellar binary systems, high eccentricities are common, and a satellite in the CD-35 2722 system would experience similar dynamics[25].

Another concern for the reality of this detection is the rotation of the host. While CD-35 B does not have the same kind of spots or chromospheric activity of stars, it may have clouds which could experience circulation, driving brightness variations over time. This effect could drive RV signals on the rotation period of the BD, or on the timescale of cloud restructuring in the atmosphere. There is some doubt that there is

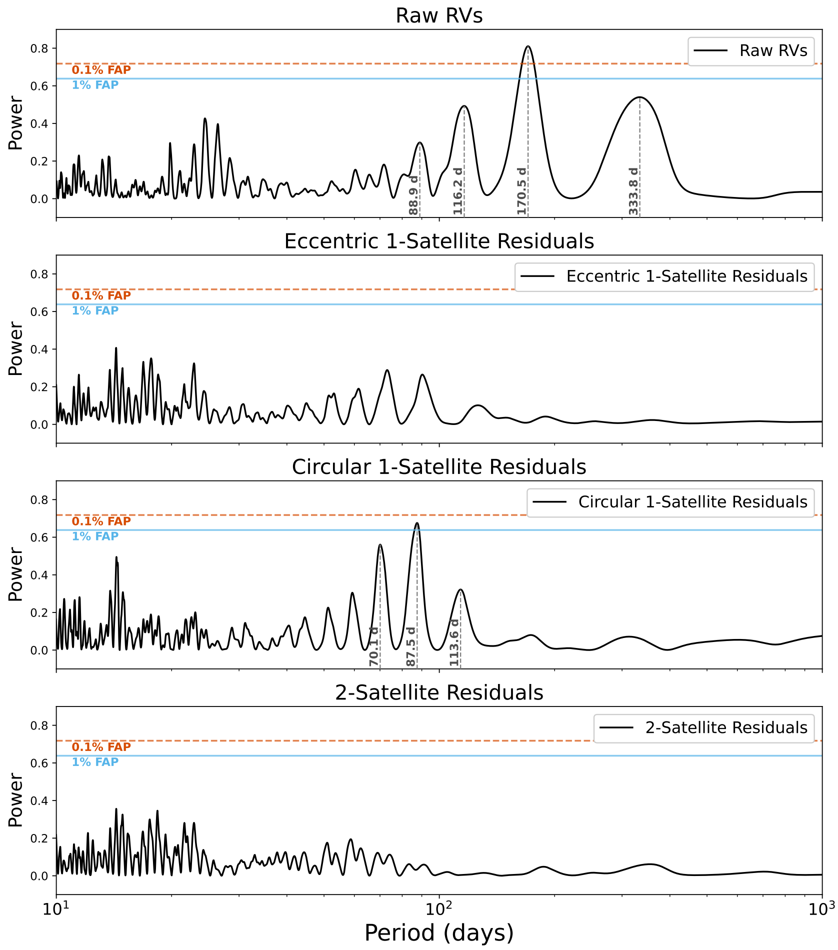

Fig. 2 Periodogram associated with the RV values seen in Figure 1 in the first panel. The other panels show periodograms for the residuals of the model fits.

substantial cloud coverage in this object, with cloudless models providing better fits during atmospheric modeling[26].

Importantly, the target is expected to rotate much faster than late-type stars tend to, due to its significantly smaller radius. We cannot directly measure the rotation period from our data and no prior measurements exist. The v$\sin i$ **has been measured to be 9.58 km/s, giving a maximum**

Table 1 Best-fit orbital parameters for one- and two-satellite models. Period, amplitude, phase, eccentricity, and longitude of periastron are the components of a Keplerian equation. Offset is not a physically meaningful parameter, it is a constant offset subtracted from the model to align the model and RV points. Jitter is a parameter that models instrumental RV errors, which is then added in quadrature with the measured RV errors.

Parameter	**1-satellite Fit**	**2-satellite Fit**
Period 1 (days)	$171.112^{+0.525}_{-0.363}$	$171.454^{+0.191}_{-0.813}$
Amplitude 1 (m/s)	$318.479^{+5.022}_{-12.718}$	$305.959^{+17.532}_{-18.540}$
Phase 1 (rad)	$4.706^{+0.083}_{-0.053}$	$2.541^{+3.660}_{-2.002}$
Eccentricity 1	$0.269^{+0.013}_{-0.037}$	$0.001^{+0.013}_{-0.001}$
Longitude of Periastron 1 (rad)	$3.459^{+0.071}_{-0.084}$	$5.647^{+0.636}_{-4.742}$
Semi-Major Axis 1 (au)	$0.200^{+0.001}_{-0.004}$	$0.195^{+0.005}_{-0.004}$
Msin i 1 (M_{Jup})	$0.918^{+0.011}_{-0.045}$	$0.869^{+0.033}_{-0.025}$
Period 2 (days)	—	$87.349^{+0.641}_{-0.451}$
Amplitude 2 (m/s)	—	$94.970^{+19.881}_{-18.887}$
Phase 2 (rad)	—	$0.543^{+1.806}_{-0.543}$
Eccentricity 2	—	$0.008^{+0.006}_{-0.008}$
Longitude 2 (rad)	—	$0.352^{+5.929}_{-0.352}$
Semi-Major Axis 2 (au)	—	$0.125^{+0.002}_{-0.000}$
Msin i 2 (M_{Jup})	—	$0.219^{+0.048}_{-0.046}$
Offset (m/s)	$-86.778^{+5.493}_{-5.684}$	$-87.86^{+7.667}_{-3.808}$
Jitter (m/s)	$1.125^{+2.902}_{-1.123}$	$2.014^{+2.041}_{-1.983}$
logZ	-144.323 ± 0.695	-141.701 ± 0.691

rotation period of 0.65 days[26]. This is significantly shorter than the long-period signal derived in this work. It also demonstrates that there is likely not a large rotational signal embedded in the data, as we do not see any strong RV changes on timescales as short as the maximum rotation period. For a photometric variability of 0.5%, there is an expected ∼50 m/s variability, on the order of the residuals of our fits[12]. We do not recover any periodic signal within the possible rotation period regime, neither in the periodograms nor in the GP modeling we performed.

Although long-timescale variability driven by magnetic activity cycles or large-scale atmospheric circulation cannot be ruled out in principle, it is unclear if they could drive such a signal. Such cycles with a period over 1 year are present in about 5% of non-active M-dwarfs, with only one object shown to have correlated RV variations on the order of 6-7 m/s[27]. Brown dwarfs can exhibit these cycles as well[28]. While such activity is potentially present in CD-35 B, it has not yet been observed, and would need to have an RV influence orders of magnitude stronger than has been seen in the past in objects of other spectral types.

At a minimum, the apparent RVs of CD-35 B show strong periodicity. This periodicity is well-modelled by an eccentric Keplerian orbit. With future follow-up observations, we hope to further confirm the detection and better characterize the orbital elements of the candidate(s). Should this signal prove legitimate, this is the first time such a hierarchical system has been observed, with a satellite orbiting a substellar object (a brown dwarf in this case), which in turn orbits a star.

This system is unique in many ways. Although some satellites around isolated BDs have been discovered in the past, they were found via direct imaging and are on orbits with significantly longer periods than 170 days[29,30]. In terms of hierarchy, perhaps the most comparable system is the Proxima Centauri / α Centauri system, which has the largest mass ratio between the planet-hosting star and its companion(s). Proxima Centauri being $\sim$0.12 $M_\odot$and both stars comprising the α Centauri binary system being $\sim$1 $M_\odot$[31], this mass ratio of about 10% is quite similar to the mass ratio between CD-35 B and the central star. However, that is a triple system composed of 3 stars, and the planets orbiting Proxima Centauri are significantly smaller than the satellite of CD-35 B, so the comparison is largely limited to this mass ratio.

The discovery and characterization of satellites will open many new lines of investigation in the realms of exoplanetary science. Planet formation theory already makes some predictions regarding satellite formation and statistics which can be refined with comparison to a real sample. Dynamicists will have access to a new dimension of system hierarchical structure. Although those discovered in this work are likely too massive to be viable hosts for it, satellites are also fascinating targets in the search for life, as they can receive tidal heating from their host planet, potentially allowing them to be habitable beyond classical stellar habitable zones[32].

The nature of this system prompts an important question: how do we define an exomoon? The satellite described here orbits a substellar host, with a minimum mass ratio of $\sim$2.5%, and is positioned as the last component in a three-tier hierarchical system. These facts would support a moon-like classification. Conversely, both the satellites and their primary are unusually massive, placing them in regimes that blur the distinctions between moons, planets, and stars.

The current IAU definition of planet states, "Objects with true masses below the limiting mass for thermonuclear fusion of deuterium (currently calculated to be 13 Jupiter masses for objects of solar metallicity) that orbit stars, brown dwarfs or stellar remnants and that have a mass ratio with the central object below the L4 / L5 instability ($M/M_{\text{central}} < 2/(25+\sqrt{621}) \approx 1/25$)) are 'planets', no matter how they formed"[33]. This definition makes no reference to system hierarchy beyond its direct host and explicitly states that planetary-mass objects orbiting brown dwarfs are planets. However, the CD-35 2722 system brings into stronger relief the difference in the future evolution between B's satellite and a hypothetical planet orbiting A. When this system reaches the same age as the current Solar System, the BD is expected to be approximately two orders of magnitude less luminous, while the central star continues shining, as bright as it is now[34,35]. This difference between a stellar host (a constant source

of radiative energy) and a substellar host has deep ramifications for the satellite itself, and it may be worth revisiting this aspect of the definition.

At present, there is no accepted definition of an exomoon, and a single criterion may prove inadequate, although this classification may also not be apt for this satellite. Perhaps we are approaching the limit of language invented to describe the Solar System, which is entirely unlike CD-35 2722. In which case, it may be best to define a new category for objects like the satellite of CD-35 2722 B, including those previously-discovered satellites orbiting BDs. With forthcoming observational facilities expected to uncover many similar systems, establishing a clear taxonomy will become increasingly important.

2 Methods

2.1 Observations and Data Reduction

The data presented are part of a survey conducted with VLT/CRIRES$^+$, a high-resolution cross-dispersed infrared echelle spectrograph, recently upgraded to greatly increase wavelength coverage, incorporate new calibration elements, and add a variety of other features[11]. We have obtained 24 epochs of observations of CD-35 B. The spectra have a resolution of ∼100,000 and span a wavelength range between 1469 and 1780 nm. The observations took place from October 2023 through February 2026. In order to achieve the S/N necessary (∼25) for this analysis, we required 10-minute exposures. They were observed in an AB nodding pattern in order to subtract the sky emission contamination that is especially strong with such long exposure times, as well as the instrumental background.

To minimize the potential for stellar contamination, the slit was aligned to be perpendicular to CD-35 B's orbital vector, maximizing the distance between the host star and any given position on the slit. Adaptive optics is also employed to sharpen the target point-spread function and further reduce contamination. Finally, because CD-35 B is on such a wide-separation orbit, there should be very little reflected light from the host star compared to its intrinsic brightness. Any potential contamination would also be reduced by the nodding subtraction, although the increased distance from the host star to the other nodding position limits the potential correction. Combining these factors, the stellar contamination is likely negligible and does not need to be modeled together with the companion's signal.

To quantitatively demonstrate the lack of contamination in our data, we fit model point-spread functions (PSFs) to the slit viewer (SV) camera images associated with our data. For our observation strategy, we guide the telescope on the host star, while offsetting the spectrograph slit to the known position of the companion. The SV images show the PSF of the host star, as reflected off of a panel surrounding the instrument's two slits. To model the host star PSF, we fit a 2D Moffat function. This function is the best approximation of the shape of the AO-corrected PSF.

Fig. 3 shows the PSF fits to the SV camera images along with a 1D radial projection to measure the contamination as a function of angular distance. The night with the worst conditions was January 30, 2024 (seeing up to 1.73 arcsec). In that worst case scenario, the potential flux ratio between the companion and the contamination is ∼13%, excluding that which is subtracted in the nodding. The effect of this can potentially be seen in Fig. 1. This epoch is the third to last point in the first year of observations, which has slightly larger error bars and is lower than the neighboring points. Even assuming this reduction in measured RV is due to the contamination, this would demonstrate that its influence is, at worst, some tens of meters per second, far lower than the measured amplitude of either signal. This PSF is also significantly worse than the average, with all other points having an apparent contamination orders of magnitude lower.

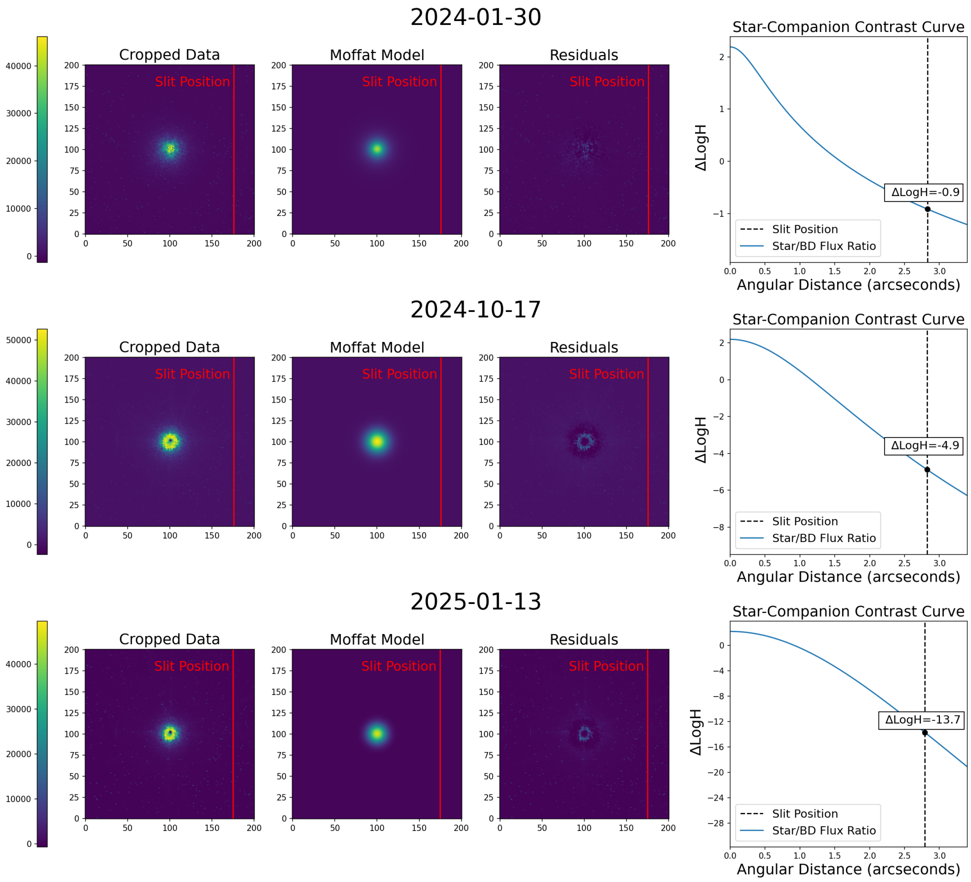

Fig. 3 Selected SV images associated with our spectra, fit with Moffat model functions. The contrast curve in the rightmost panels shows the log-scale H-band flux ratio (ΔLogH) between the host star and CD-35 B as a function of angular distance from the star, specifically marking the position of the slit. This is based on the relative diminishment of the model and the contrast of the star and companion given in the discovery paper [7]. The first row is the night with the worst observing conditions, and shows a maximum contamination of ∼15%. The other two selected epochs are under better weather conditions. The dark pixels in the center of the real PSF are due to saturation of the detector. These points are masked when fit, but not having central pixels does complicate the fit, as can be seen in the residual ring for the two good weather observations. This effect should not significantly affect the results at separations as distant as the slit.

To reduce the data, we used the official ESO pipeline, using the cr2res recipes (version 1.6.10)[2]. This reduction was performed using the default settings of the pipeline.

When reducing nodding observations, it is common practice to not only subtract the nodding frames to remove sky contamination, but also to combine the extracted

[2] https://www.eso.org/sci/software/pipelines/cr2res/cr2res-pipe-recipes.html

spectra into a single combined spectrum in order to improve S/N. In this work, however, we choose to use the individual nodding frames as separate observations through the RV extraction phase, after which they are binned into a single RV measurement per night of observation. This is motivated by the need for a wavelength solution that maintains the highest possible accuracy. CRIRES$^+$is not a stabilized instrument, so it is not guaranteed that the wavelength solutions between the A and B nodding frames are the same, and minute-to-minute drifts are known to exist within the instrument. Therefore, we choose to eschew the S/N gain of spectral combination for the ability to recalibrate the wavelength solutions separately for the two nodding positions.

In short, by using the frames separately, we lose RV precision through S/N loss, but gain higher-precision wavelength calibrations for each frame. Then, assuming the true RV of the target is constant over the short time between the two nodding positions, we can bin these two measurements with a weighted mean and associated error propagation to produce a single, higher-precision RV measurement for each night. The precision gain of this method is approximately 10%, as can be seen in Fig. 4.

2.2 Radial Velocity Extraction: `viper`

To extract the RVs, we use the RV pipeline `viper`[17,18] which employs a forward-modeling approach. The code offers the option to co-add all spectra to create a telluric-free, high S/N template of the target. This template serves as a reference for the calculation of the RV values. The creation of the template is an iterative process. In the first step, the telluric-corrected spectra are co-added after shifting them into the same barycentric rest frame. In a next step, this template can be used as an input for a second round of template creation, allowing the code to correct for RV shifts between the different observations, improving the next template. The results in this work are based on two template iterations, as subsequent iterations showed little to no change in the extracted RVs.

Since the parameters vary strongly with wavelength, the RVs are calculated separately for each spectral order. The final RV is the weighted mean of the individual RV values of all spectral orders. The corresponding final uncertainty is given by this equation from Köhler et al. (2025)[18]:

$$\epsilon_{\mathrm{RV}} = \sqrt{\frac{1}{N_o - 1} \cdot \frac{\sum \epsilon_o^{-2} \cdot (\mathrm{RV}_o - \mathrm{RV})^2}{\sum \epsilon_o^{-2}}} \tag{1}$$

Here, N_o is the number of orders included, ϵ_o is the RV variance of a given order as given by that order's covariance matrix, RV_o is the RV of a given order, and RV is the weighted mean RV. For more details regarding the RV calculation, see Köhler et al. (2025)[18].

In `viper`, all parameters are optimized simultaneously, including the wavelength solution. In our case, it uses the telluric lines as a reference frame, as these lines are expected to be stable to about 10 m/s[36]. However, not all orders contain sufficient telluric lines for a high-quality recalibration. These orders are excluded from the calculation, as this failed calibration produces highly erratic results.

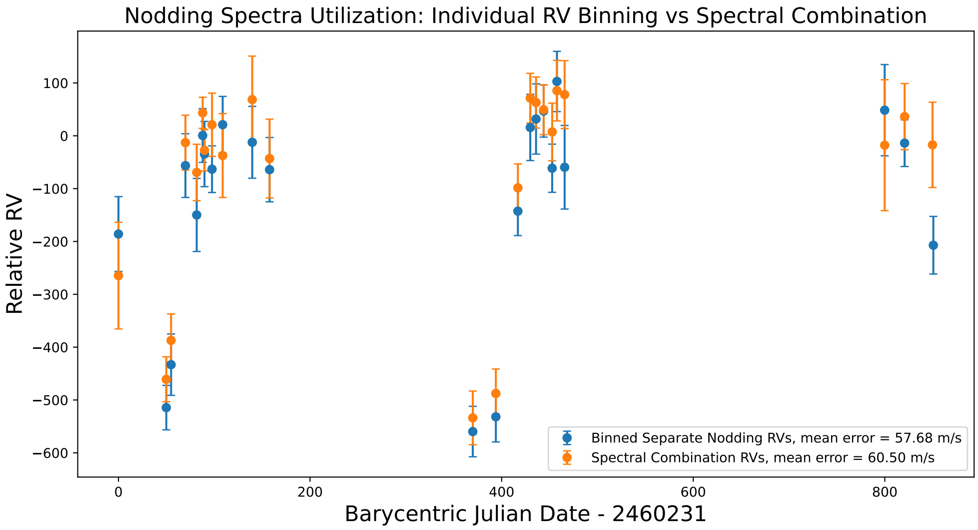

Fig. 4 Comparison of final RV calculation methods. The blue points are the favored method, in which we calculate separate RVs for both nodding positions, then bin the results. The orange points are based on combining the two nodded spectra before calculating the RV. The precision improvement with the former method is ∼10%, as seen in the mean error in the legend.

2.3 Keplerian Orbit Fitting: `EMPEROR`

After obtaining the RVs from `viper`, they are used as input for the Keplerian orbit-fitting code `EMPEROR` (see Peña et al. 2025 for details on its underlying mathematics and algorithm)[37]. This code employs adaptive parallel tempering MCMC fitting through reddemcee[38] to quickly probe the large parameter space of possible orbits. It iterates through Keplerian models of different degrees (i.e., one orbiting body, two orbiting bodies, etc.) until the Nth Keplerian model is not a significantly better fit than the last.

When using `EMPEROR`, we use a different parameterization of the orbital elements than the one presented in the results. Instead of directly probing the eccentricity (e) and longitude of periastron (ω), as reported, we fit $\sqrt{e}\sin\omega$ and $\sqrt{e}\cos\omega$. This generally favors lower-eccentricity orbits and prevents the model from overfitting the data with high-eccentricity, short-period orbits in higher order Keplerian models[39]. High-eccentricity orbits tend to be capable of fitting a Keplerian signal to any given dataset, even where none exists. We convert these parameters back to eccentricity and longitude of periastron when reporting them, as those quantities are more easily conceptualized independently.

For the initial run, we employ wide uninformative priors to avoid biasing the fit. From that run, we identify symmetrical solutions in the posteriors, as the code cannot define which signal should be "satellite 1" or "satellite 2", just that both signals exist. We then narrow the period prior for "satellite 1" to only include the strong, long-period peak, limiting "satellite 2" to shorter-period signals.

When we separate these signals into greater than or less than 150 days, we always recover the strong ∼170 day period in the long regime. However, in the short-period regime, there are degeneracies in the posterior, showing multiple potential secondary signals. These posteriors are in the first panel of Fig. 5. In order to compare which model fits best, we break these posteriors into multiple windows covering each period separately in order to get a Bayesian evidence estimation for each solution. There are 4 possible solutions at periods of 14 days, 70 days, 88 days, and 115 days. These periods are all aliases of each other with our current sampling, due to the two sets of observations being almost exactly a year apart. Observing this target again, avoiding this ∼1 year mean time difference will help break this degeneracy.

The 14-day period model is somewhat of a special case, as the window encompassing it showed, in itself, a highly multimodal peak around this solution spanning 13 to 17 days. This leads us to believe that periods this short are simply too difficult to constrain with our current dataset. Below this ∼20 day period limit, there are many solutions which could potentially fit, but these are likely artifacts of our low-cadence sampling. Periods that are very short compared to the sampling of the data are often capable of resolving the residuals of an imperfect fit, which, in this case, is the 1-satellite circular orbit fit. Thus, we reject the models in this period window.

For the other three windows, we must rely on the evidence estimations to determine the most favored model, as the posteriors are all singular and approximately gaussian in these windows. Based on the derived evidences, the 88-day model is about 4.5x more likely than the 115-day model, and 6x more likely than the 70-day model. While this difference is not negligible, it is not sufficient to claim with any degree of certainty a known period for the potential secondary signal.

The full posteriors for all windowed fits are shown in Fig. 5. The best-fit models and their residuals are shown in Fig. 6.

We further used `EMPEROR` to search for any additional signals in the RV data, which may be correlated to the rotation of the BD or other effects independent of an orbiting satellite. We used Gaussian Processes (GPs)[40] with `celerite2`[41] to search for any signal which could be correlated to the rotation of the BD. We used the Rotation kernel and Simple Harmonic Oscillator (SHO) kernel to search for the effects of spots, faculae, differential rotation, and granulation[41,42].

The Rotation kernel is capable of modeling spots, faculae, and differential rotation, all of which have have signals associated with Q0 hyperparameter values of < 10. Our fit recovered a largely flat posterior in Q0, favoring larger values up to 10,000, indicating that we do not recover any of these rotational signals. Such high values of Q0 mean that the signal is best fit with pure sinusoids, which could be degenerate with Keplerian solutions. Likewise, we used the SHO kernel to model potential granulation (or a similar effect, such variable cloud coverage), and again recovered flat posteriors in Q spanning $1/\sqrt{2}$ to 1. If granulation were a strong noise factor, the Q value should be within this range, and we identify no strong signal here. These GP posteriors are shown in Fig. 7.

Overall, glean two important insights from this analysis. First, it is less likely that the observed RV signal could be caused by intrinsic changes with the BD, as we recover no potential signals at appropriate hyperparameter values. Second, as we are unable to model the remaining jitter after fitting the Keplerians, we thus assume an indepdendent gaussian noise model for this work.

2.4 Orbital Stability Analysis: REBOUND & the Roche Limit

To confirm the stability of the proposed satellite system(s), we employed the N-body simulation code REBOUND. The code includes a suite of tools for integrating a wide array of system configurations, including the inclusion of moons/satellites.

Initial tests revealed the two-satellite model to be highly unstable, with one of the two satellites being ejected in some hundreds of years in most configurations. To test this model, we used the IAS15 integrator, as it can accurately simulate this high degree of chaos[43]. Looking specifically at the BD-satellite component of the system, the only meaningful variable for the satellites' orbits are their inclinations, due to the orbits' circularity. We examine the parameter space of both inclinations separately, rather than a single parameter of their relative inclination, as this allows us to make use of the known $\mathrm{m}\sin i$ of both satellites, so that the implied true mass can be factored into the stability analysis. Inclination values within 5° of 0° and 180° are excluded due to the rapidly increasing mass of the satellite.

Across this inclination parameter space, we use the MEGNO value to determine the stability of the system. This value converges to 2 when a system is stable, and is higher for unstable systems. We integrate the BD-satellite system for only 5000 years, as MEGNO is capable of determining long-term stability without overly long N-body integrations. We find a single strip of stable configurations, shown in Fig. 8 This shows that the two-satellite model is only stable when the two satellites are on counter-rotating orbits and are within $\sim 20^\circ$ of coplanar. This requirement for stability has been observed in exoplanet stability studies in the past, specifically in cases of MMR[44]. As discussed in the main article, this configuration is significantly more difficult to form than the 1-satellite model, and leads us to disfavor this model.

This initial analysis only considers the BD-satellite system, ignoring the perturbation from the host star. However, we can use this result to significantly narrow the parameter space necessary to model the stability of the overall system. If the satellites are coplanar, then we are only concerned with the overall inclination and longitude of their orbits around the BD. This leaves a 2-dimension parameter space, covering 0° to 180° in inclination and 0° to 360° in longitude. We cannot make further use of symmetry, as it is possible that the stability of the system is affected by which satellite is prograde with respect to the BD orbit, and which is retrograde. Simulating the entire Star-BD-Satellites system requires significantly longer integration times, as the BD orbital period is around 5000 years. This means that we cannot as narrowly probe all parameter space, and are forced to use much wider bins to avoid an excessive number of simulations. We integrate this configuration for 100,000 years, around 20 BD orbits, which should be sufficient for the MEGNO value to show that the perturbation of the host star can cause the system to be unstable.

In the lower-resolution stability map, Fig. 9, we find islands of instability, when the satellite orbits are approximately coplanar with the BD orbit. There are also strips of instability for inclinations that would give a nearly face-on orbit, indicating that the satellites have a maximum mass for which orbits are stable. These results further challenge the plausibility of this model, as even in the regimes where the BD-satellite system is internally stable, the star's influence can destabilize the system on relatively short timescales.

We now discuss the stability analysis of the one-satellite model. It has been shown that coplanar, prograde orbits are the most unstable for satellites[45]. We can make use of this fact to test the general stability of this configuration while ruling out large areas of parameter space. If the system is stable when the satellite is coplanar and prograde, it will also be stable in most other configurations. This leaves only a single variable: the argument of periapsis. We therefore simulate this model across an array values for the argument of periastron, relative to that of the BD's to simplify the geometry. We integrate this system three times, for 30, 300, 3,000 orbits. By doing so, we can show longer-term stability. If all three simulations agree, that shows that the system does not evolve into an unstable state over these timescales, and is instead either immediately unstable or stable over long timescales. We find that this system is generally stable for most values of this orbital element, although near $\pm 115^{\circ}$ we find small islands of instability, as can be seen in Fig. 10. While the existence of these islands is interesting, and warrants further study, we leave that for a future work, as the core result of relevance to this work is the general stability of the model. We do see that the three simulations generally agree in their results, indicating that short-term instability is possible, but instability is not likely to emerge in the long term. The 3,000 orbit case shows some instability around a value of two, but as this integration covers 10% of the total system lifetime, without the system experiencing large changes. This likely reflects accumulated numerical instability over the long integration, rather than dynamical instability in the system.

While `REBOUND` is capable of simulating collisions and tides, we exclude such effects from the analysis to limit computation times. We perform such calculations ourselves, in order to be sure that the satellite's orbit is not too close to the BD to survive.

The Roche limit depends on the radius of the host, and the densities of both host and satellite. Using isochrones with CD-35 B's age and mass, we

find a radius of 1.2 R_{Jup}, and thus 29 g/cm^3 for the mean density[9,46]. For the possible satellites, we conservatively estimate that they both have the same density as Saturn (0.687 g/cm^3). It is impossible to say how accurate this approximation is, as we have no information regarding the satellite radii, but this should be a realistic underestimate of the true densities. If the satellites are outside of this upper limit on the Roche limit at this underestimated density, they must also clear this criterion at their true densities. We calculate a maximum Roche limit of 8.4 $R_{CD\text{-}35b}$, which is only 0.0064 AU, well below the periapse distance of any satellite in either model.

2.5 Verifying the periodicity of the signal

On initial inspection, the period of the outer/lone satellite could be seen as suspicious, as it is relatively near 182.5 days, half an Earth year. If there are imperfect corrections applied to, say, the barycentric velocity or instrument profile[47], this could create a false signal with a true period of 365 days, which could be aliased to the 182.5 days by sampling. However, we have extensively investigated this possibility and have found no correlations between the derived RVs and the applied barycentric correction. We have also looked at atmospheric parameters (seeing, precipitable water vapor, etc), which could also be periodic in yearly weather patterns, and again found no correlations with our data. The derived large satellite period is also very well-constrained to $169.45^{+1.1}_{-1.06}$ days (in the 2-satellite model), meaning 182.5 days is off by approximately 11σ. Thus, while this period could seem suspicious, it is highly improbable that it is due to any unaccounted for Earth-based effect.

Further, we compared our results to GLS periodograms made using the model parameters fit by `viper` in conjunction with the RVs, to see if they shared any periodicity with the RVs themselves. No correlation can be found, with no significant periodicities present in these parameters, and even the insignificant peaks do not align with the derived periods of the satellites. These periodograms can be compared in Fig. 11. Specifically, the "instrument profile" periodogram could be influenced by the rotation of the target. We assume that the primary contributor to the line profile is instrumental, hence the name, but it is theoretically possible that if there are real changes in the line profile of the object, they would manifest here. However, no periodicity is recovered for this variable, meaning it is unlikely for rotational modulation of line profiles to be a significant driver of the RV variation. Of these periodograms, the one with the strongest peaks is the one for precipitable water vapor, but those peaks are much nearer to an Earth year and its aliases, denoting seasonal weather cycles, rather than the periods of our proposed satellites.

We have also performed an orbital fit in which we do not combine the RV values from the eleven included spectral orders. We bin the RV values for each order across the two nodding frames, but leave each order as a separate measurement, giving us 11 measurements in a given night. Individually, these points have significantly higher errors than the combined points used for the main analysis. However, by leaving them separate, we can see if there exists any order with especially low errors that may be

too heavily weighted is driving the fit, or if the points are distributed about mean values which continue to show periodicity. In this case, the latter appears to be correct, as we are able to recover an almost identical best-fit model which the orders are dispersed about. The only significant difference between the models is a slightly amplified eccentricity in the individual-orders case, which is 0.3 instead of 0.27. Both models can be seen in Fig. 12, along with these order-separated points. In this plot, it can be seen that Order 11 is relatively unstable. Despite this, we include it in the main analysis because it is still stable compared to those orders we have excluded, and we prefer to err on side of caution and include as many orders as possible. This order's high error measure mitigates its effect on the weighted binning, in any case.

There are four specific epochs that are key to this result, which constitute the limited sampling of the lower end of our orbital fits. From our examination, there is nothing unique about these points beyond their low RV. They were all taken in excellent weather conditions, as were many of the points with higher RVs. The points have no outlying instrumental parameters, such as detector temperature, grating position, S/N, or telescope position. These points also come in pairs, with each point having a correlated low RV point as well. If we exclude any one of these points, we recover the exact same signal because of the neighboring point containing the same information as the one removed. **It is also the case that when we separate each epoch into its individual orders, there is clear general agreement on a significantly lower RV for these four epochs**. While a more complete orbital sampling would be ideal, we have found no reason to doubt the validity of these four crucial points.

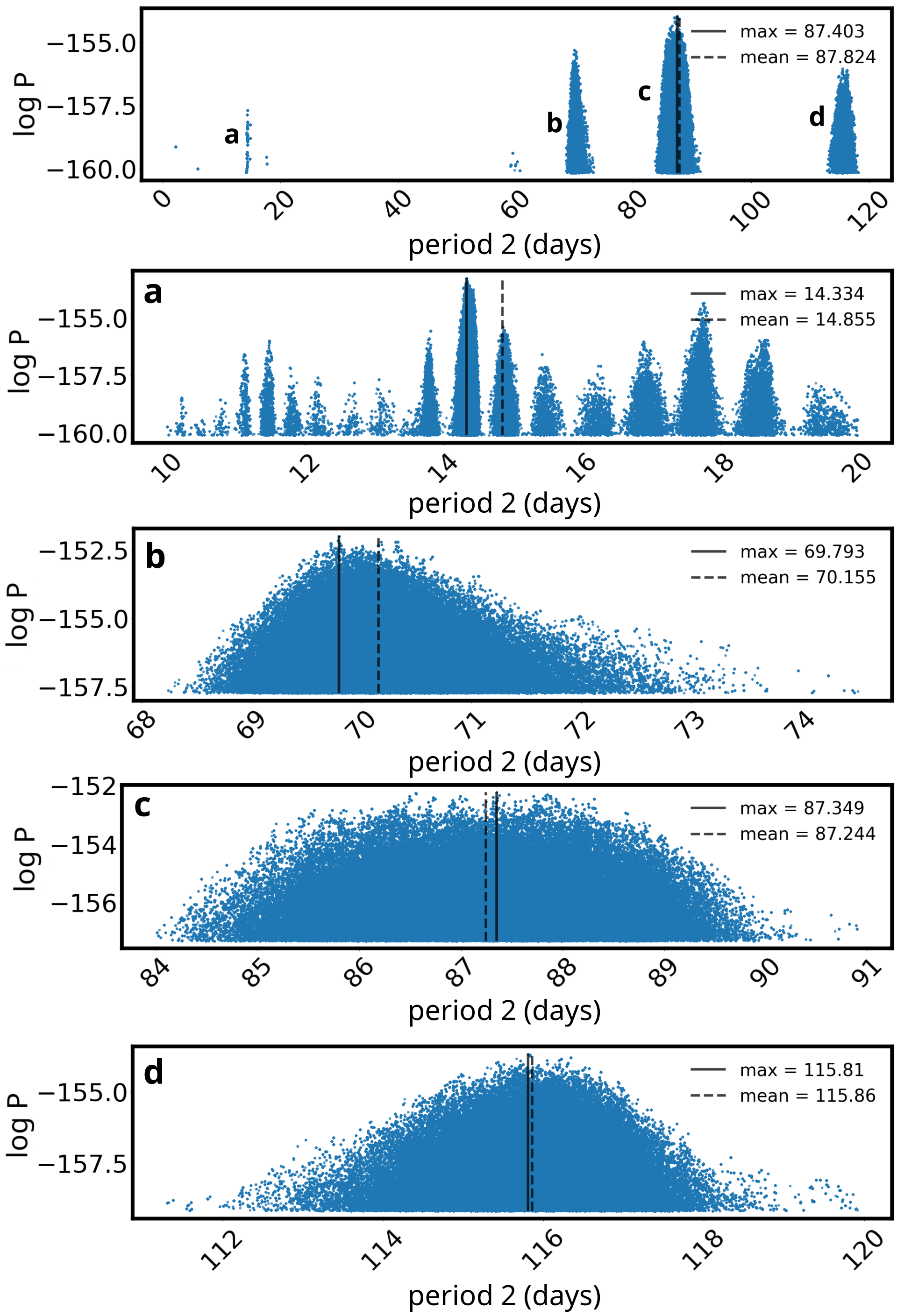

Fig. 5 Period posteriors for the main and windowed 2-satellite model fits. The first panel shows all the periods recovered for the second signals. The other panels are windowed fits for each of the peaks seen in the first panel, and are labeled 1-4 accordingly.

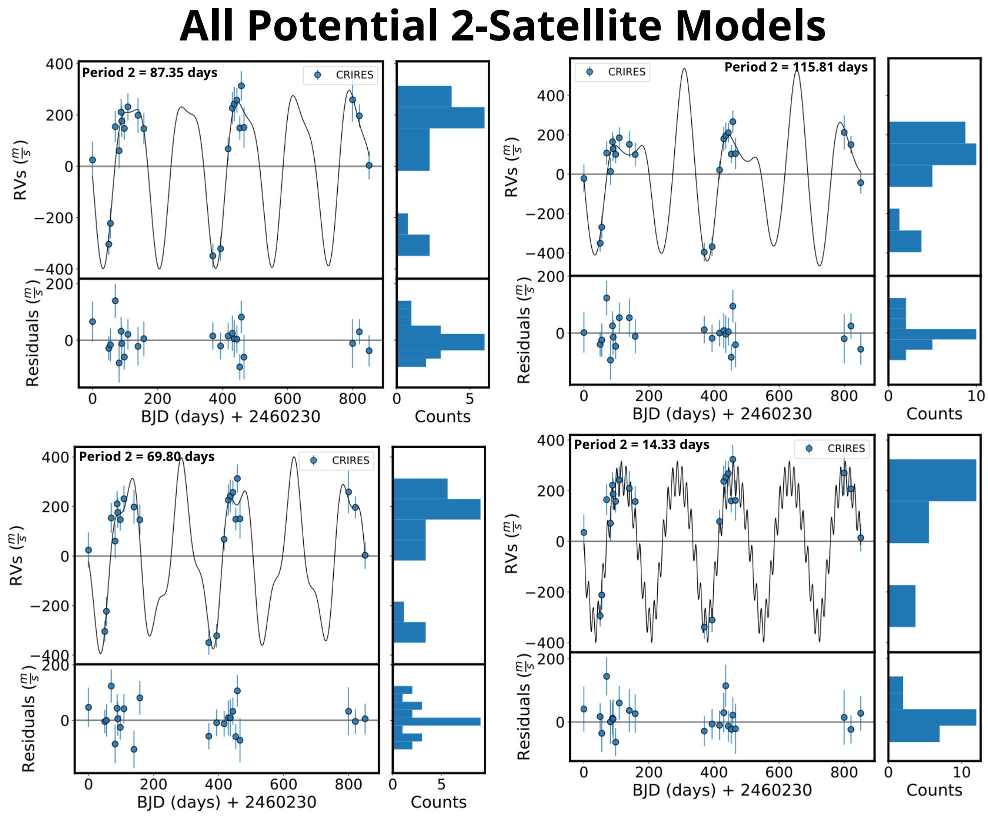

Fig. 6 All high-evidence 2-satellite models. One can see the reason for distrusting the 14-day model, as these high-frequency oscillations would appear more likely to be an artifact of the sampling, rather than a true signal we could recover from this data.

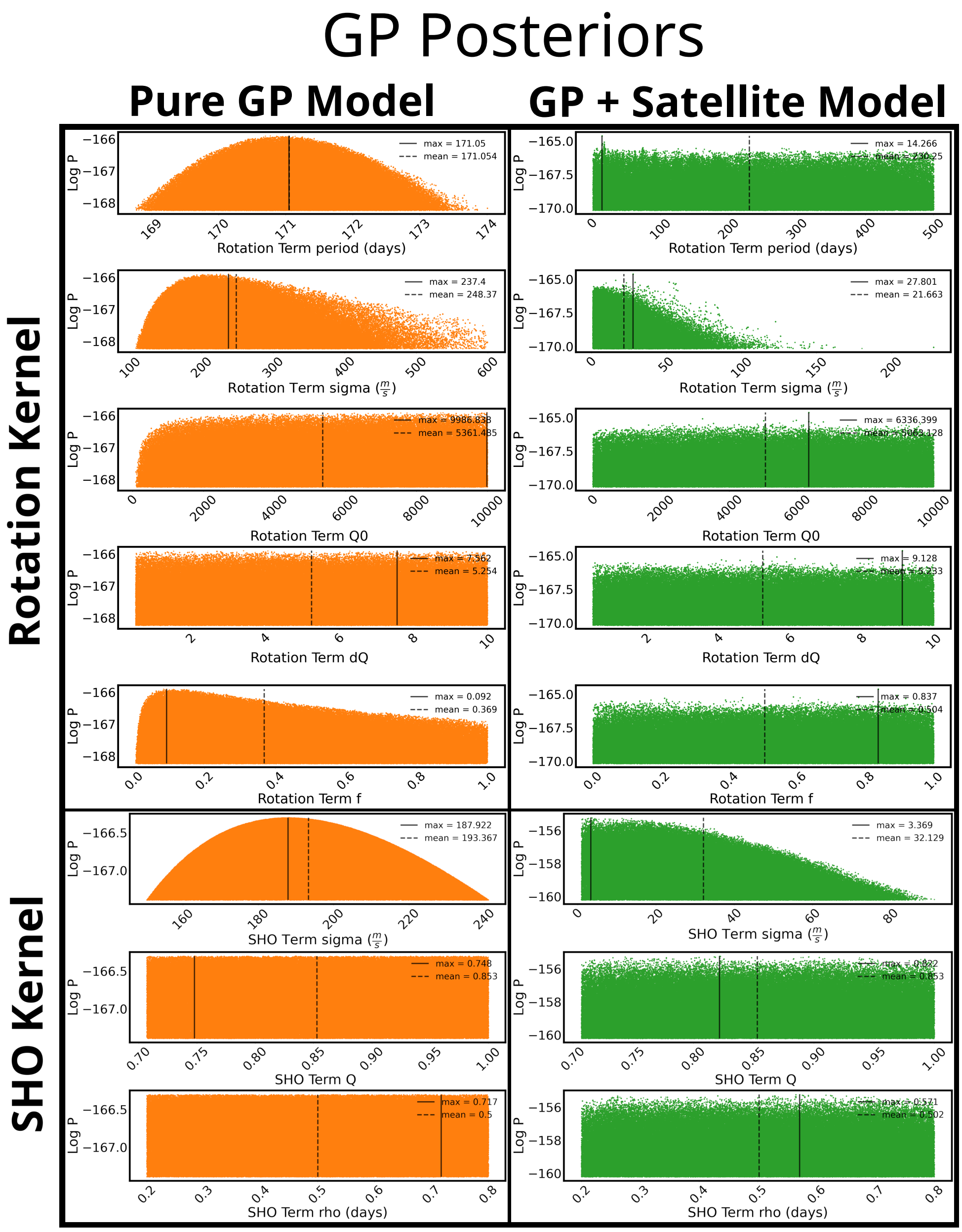

Fig. 7 Posteriors for Gaussian Process fitting. The left column shows that we do not successfully recover any signals indicative of activity. The right column shows a lack of a meaningful noise model when combining GPs with Keplerian model fitting.

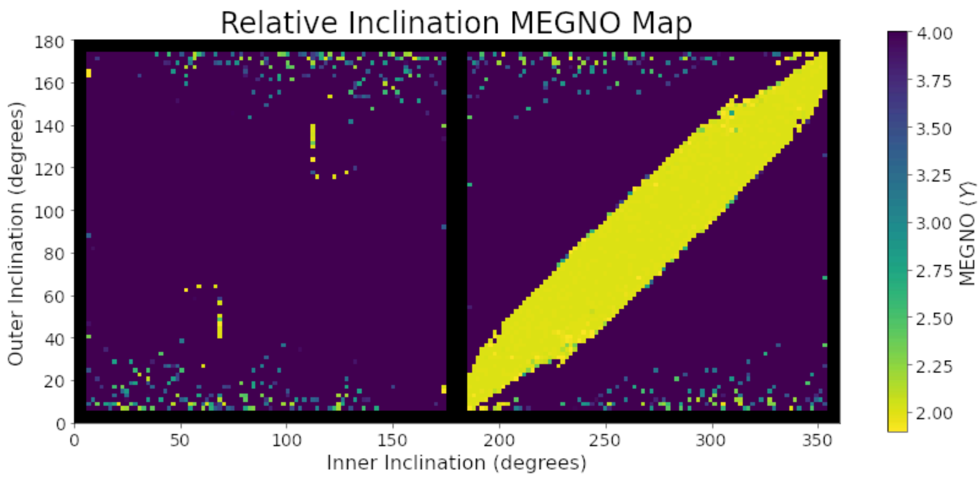

Fig. 8 MEGNO map showing the regions of stability for the best-fit two-satellite model. For stable systems, the MEGNO converges to 2, while all other values are considered unstable. The x-axis covers the inclination angles of the inner satellite, while the y-axis is the inclination of the outer satellite. The y-axis is limited to a maximum value of 180º because higher values will result in duplicated configurations.

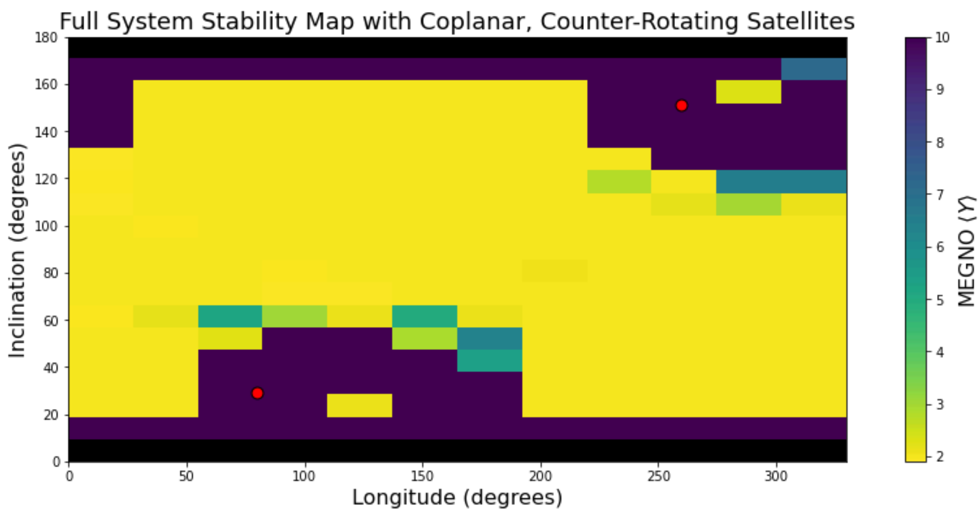

Fig. 9 MEGNO map showing the regions of stability for the two-satellite model, with both satellites on coplanar, counter-rotating orbits. Both satellites share the same longitude, with the outer satellite being inclined 180° to the inclination given by the y-axis. The red dots indicate the orbits which are coplanar with the BD's orbit around the star. There we see islands of instability, along with strips of instability at nearly face-on orbits.

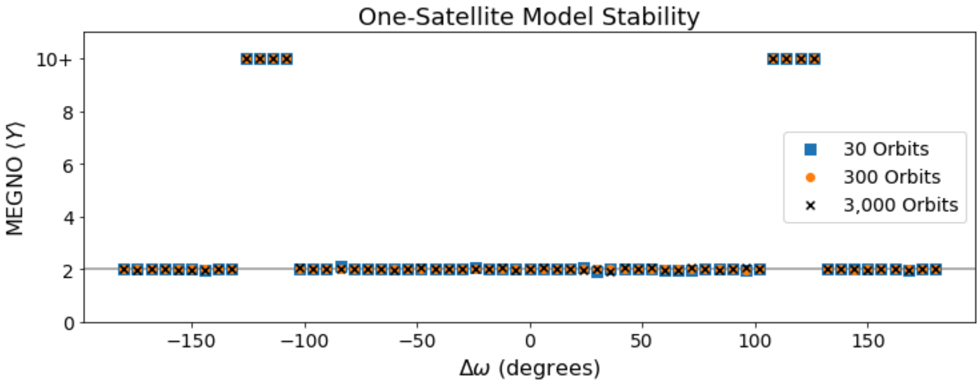

Fig. 10 MEGNO curve showing the stability of the one-satellite model, depending on the satellite's initial argument of periapsis. The horizontal line marks the value of maximum stability, while a maximum value has been placed at 10, at and above which orbits are highly unstable, no matter the true MEGNO value.

Generalized Lomb–Scargle Periodograms for RV and Mean Non-RV Viper Parameters

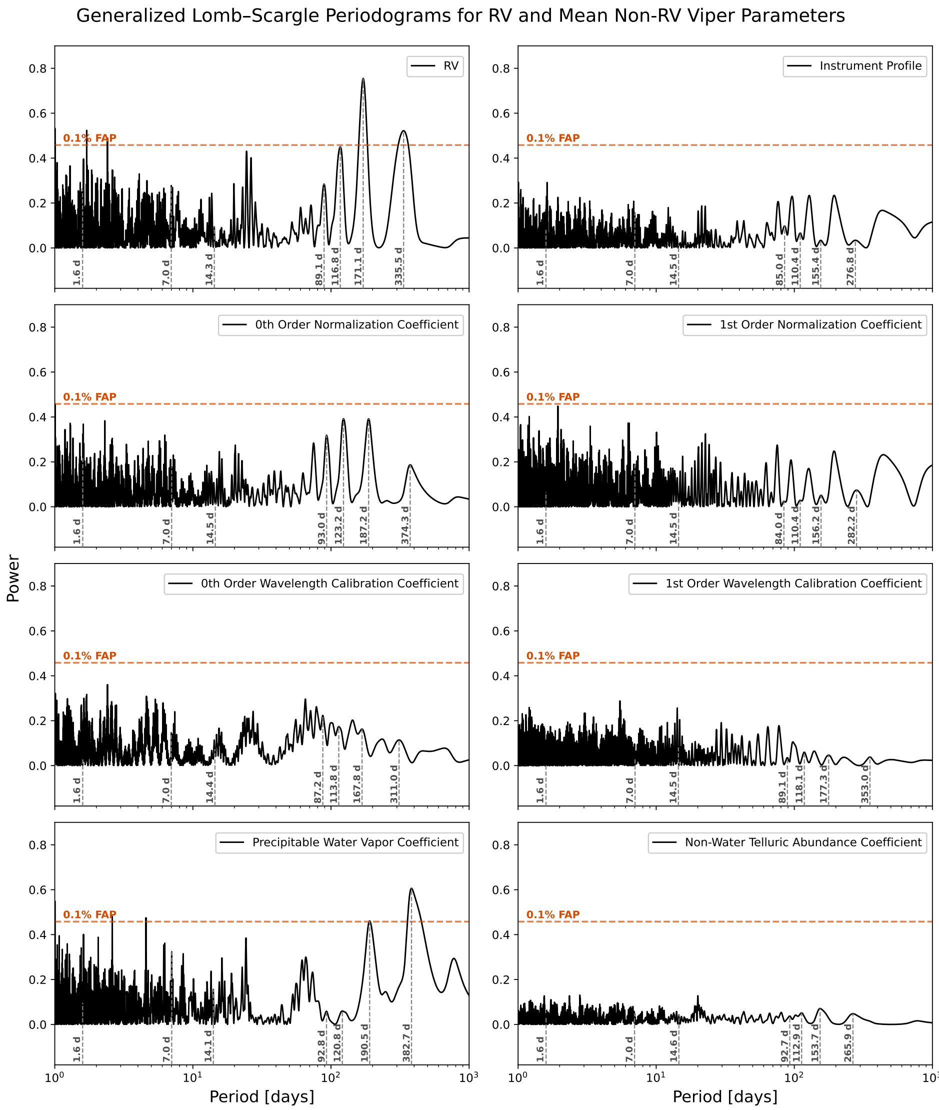

Fig. 11 GLS periodograms for all `viper` outputs. The first panel is the same as Fig. 2 above, and is reiterated for comparison. The spectra have been normalized and wavelength calibrated with 2nd order polynomials, hence the paired coefficients, but the 2nd order coefficients in both cases do not significantly vary, and are thus omitted for readability. The dashed lines in each panel are the maxima located nearest to those shown in the RV panel, to show that none repeat the same periodicities.

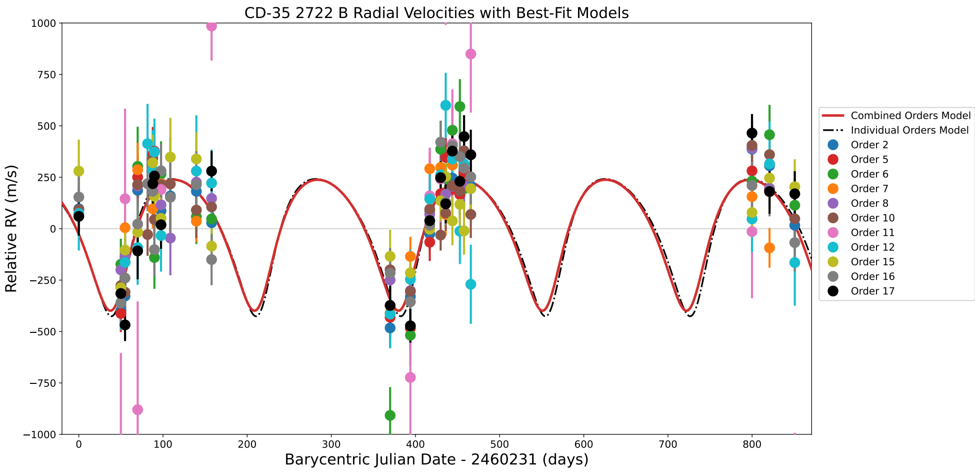

Fig. 12 RV curve showing each order independently, instead of combined as employed in the main analysis. The best-fitting model from the main analysis is compared to the model which best fits these points.

References

[1] Schneider, J., Dedieu, C., Le Sidaner, P., Savalle, R., Zolotukhin, I.: The extrasolar planets encyclopaedia: A database for exoplanets and their host stars. Astronomy & Astrophysics **532**, 79 (2011) https://doi.org/10.1051/0004-6361/201116713

[2] Lazzoni, C., Zurlo, A., Desidera, S., Mesa, D., Fontanive, C., Bonavita, M., Ertel, S., Rice, K., Vigan, A., Boccaletti, A., Bonnefoy, M., Chauvin, G., Delorme, P., Gratton, R., Houllé, M., Maire, A.L., Meyer, M., Rickman, E., Spalding, E.A., Asensio-Torres, R., Langlois, M., Müller, A., Baudino, J.-L., Beuzit, J.-L., Biller, B., Brandner, W., Buenzli, E., Cantalloube, F., Cheetham, A., Cudel, M., Feldt, M., Galicher, R., Janson, M., Hagelberg, J., Henning, T., Kasper, M., Keppler, M., Lagrange, A.-M., Lannier, J., LeCoroller, H., Mouillet, D., Peretti, S., Perrot, C., Salter, G., Samland, M., Schmidt, T., Sissa, E., Wildi, F.: The search for disks or planetary objects around directly imaged companions: a candidate around dh tauri b. Astronomy amp; Astrophysics **641**, 131 (2020) https://doi.org/10.1051/0004-6361/201937290

[3] Oza, A.V., Johnson, R.E., Lellouch, E., Schmidt, C., Schneider, N., *et al.*: Sodium and potassium signatures of volcanic satellites orbiting close-in gas giant exoplanets. The Astrophysical Journal **885**, 168 (2019) https://doi.org/10.3847/1538-4357/ab48e2

[4] Kipping, D., Yahalomi, D.A.: A search for transit timing variations within the exomoon corridor using kepler data. Monthly Notices of the Royal Astronomical Society **518**(3), 3482–3493 (2022) https://doi.org/10.1093/mnras/stac3360

[5] Kipping, D., Bryson, S., Burke, C., Christiansen, J., Hardegree-Ullman, K., Quarles, B., Hansen, B., Szulágyi, J., Teachey, A.: An exomoon survey of 70 cool giant exoplanets and the new candidate kepler-1708 b-i. Nature Astronomy **6**(3), 367–380 (2022) https://doi.org/10.1038/s41550-021-01539-1

[6] Mayor, M., Queloz, D.: A Jupiter-mass companion to a solar-type star. **378**(6555), 355–359 (1995) https://doi.org/10.1038/378355a0

[7] Wahhaj, Z., Liu, M.C., Biller, B.A., Clarke, F., Nielsen, E.L., Close, L.M., Hayward, T.L., Mamajek, E.E., Cushing, M., Dupuy, T., Tecza, M., Thatte, N., Chun, M., Ftaclas, C., Hartung, M., Reid, I.N., Shkolnik, E.L., Alencar, S.H.P., Artymowicz, P., Boss, A., de Gouveia Dal Pino, E., Gregorio-Hetem, J., Ida, S., Kuchner, M., Lin, D.N.C., Toomey, D.W.: The Gemini NICI Planet-finding Campaign: Discovery of a Substellar L Dwarf Companion to the Nearby Young M Dwarf CD-35 2722. **729**(2), 139 (2011) https://doi.org/10.1088/0004-637X/729/2/139 arXiv:1101.2893 [astro-ph.SR]

[8] Bowler, B.P., Blunt, S.C., Nielsen, E.L.: Population-level eccentricity distributions of imaged exoplanets and brown dwarf companions: Dynamical evidence for distinct formation channels*. The Astronomical Journal **159**(2), 63 (2020)

https://doi.org/10.3847/1538-3881/ab5b11

[9] Gratton, R., Bonavita, M., Mesa, D., Zurlo, A., Marino, S., Desidera, S., D'Orazi, V., Rigliaco, E., Squicciarini, V., Nogueira, P.H.: Implications of the discovery of AF Lep b. The mass-luminosity relation for planets in the β Pic Moving Group and the L-T transition for young companions and free-floating planets. **684**, 69 (2024) https://doi.org/10.1051/0004-6361/202348012 arXiv:2402.09067 [astro-ph.EP]

[10] Lazzoni, C., Desidera, S., Gratton, R., Zurlo, A., Mesa, D., Ray, S.: Detectability of satellites around directly imaged exoplanets and brown dwarfs. **516**(1), 391–409 (2022) https://doi.org/10.1093/mnras/stac2081 arXiv:2207.07569 [astro-ph.EP]

[11] Dorn, R.J., Bristow, P., Smoker, J.V., Rodler, F., Lavail, A., Accardo, M., van den Ancker, M., Baade, D., Baruffolo, A., Courtney-Barrer, B., Blanco, L., Brucalassi, A., Cumani, C., Follert, R., Haimerl, A., Hatzes, A., Haug, M., Heiter, U., Hinterschuster, R., Hubin, N., Ives, D.J., Jung, Y., Jones, M., Kaeufl, H.-U., Kirchbauer, J.-P., Klein, B., Kochukhov, O., Korhonen, H.H., Köhler, J., Lizon, J.-L., Moins, C., Molina-Conde, I., Marquart, T., Neeser, M., Oliva, E., Pallanca, L., Pasquini, L., Paufique, J., Piskunov, N., Reiners, A., Schneller, D., Schmutzer, R., Seemann, U., Slumstrup, D., Smette, A., Stegmeier, J., Stempels, E., Tordo, S., Valenti, E., Valenzuela, J.J., Vernet, J., Vinther, J., Wehrhahn, A.: CRIRES$^+$ on sky at the ESO Very Large Telescope. Observing the Universe at infrared wavelengths and high spectral resolution. **671**, 24 (2023) https://doi.org/10.1051/0004-6361/202245217 arXiv:2301.08048 [astro-ph.IM]

[12] Vanderburg, A., Rappaport, S.A., Mayo, A.W.: Detecting exomoons via doppler monitoring of directly imaged exoplanets. The Astronomical Journal **156**(5), 184 (2018) https://doi.org/10.3847/1538-3881/aae0fc

[13] Horstman, K., Ruffio, J.-B., Batygin, K., Mawet, D., Baker, A., Hsu, C.-C., Wang, J.J., Wang, J., Blunt, S., Xuan, J.W., Xin, Y., Liberman, J., Agrawal, S., Konopacky, Q.M., Blake, G.A., O, C.R.D., Bartos, R., Bond, C.Z., Calvin, B., Cetre, S., Delorme, J.-R., Doppmann, G., Echeverri, D., Finnerty, L., Fitzgerald, M.P., Jovanovic, N., Lopez, R., Martin, E.C., Morris, E., Pezzato, J., Ruane, G., Sappey, B., Schofield, T., Skemer, A., Venenciano, T., Wallace, J.K., Wallack, N.L., Wizinowich, P.: RV measurements of directly imaged brown dwarf GQ Lup B to search for exo-satellites (2024). https://arxiv.org/abs/2408.10299

[14] Ruffio, J.-B., Horstman, K., Mawet, D., Rosenthal, L.J., Batygin, K., Wang , J.J. Millar-Blanchaer, M., Wang , J. Fulton, B.J., Konopacky, Q.M., Agrawal, S., Hirsch, L.A., Howard, A.W., Blunt, S., Nielsen, E., Baker, A., Bartos, R., Bond, C.Z., Calvin, B., Cetre, S., Delorme, J.-R., Doppmann, G., Echeverri, D., Finnerty, L., Fitzgerald, M.P., Jovanovic, N., López, R., Martin, E.C., Morris, E., Pezzato, J., Ruane, G., Sappey, B., Schofield, T., Skemer, A., Venenciano, T.,

Wallace, J.K., Wallack, N.L., Wizinowich, P., Xuan, J.W.: Detecting exomoons from radial velocity measurements of self-luminous planets: Application to observations of hr 7672 b and future prospects. The Astronomical Journal **165**(3), 113 (2023) https://doi.org/10.3847/1538-3881/acb34a

[15] Vanderburg, A., Rodriguez, J.E.: First Doppler Limits on Binary Planets and Exomoons in the HR 8799 System. **922**(1), 2 (2021) https://doi.org/10.3847/2041-8213/ac33b4 arXiv:2110.14650 [astro-ph.EP]

[16] Palma-Bifani, P., Chauvin, G., Bonnefoy, M., Rojo, P.M., Petrus, S., Rodet, L., Langlois, M., Allard, F., Charnay, B., Desgrange, C., Homeier, D., Lagrange, A.-M., Beuzit, J.-L., Baudoz, P., Boccaletti, A., Chomez, A., Delorme, P., Desidera, S., Feldt, M., Ginski, C., Gratton, R., Maire, A.-L., Meyer, M., Samland, M., Snellen, I., Vigan, A., Zhang, Y.: Peering into the young planetary system AB Pic. Atmosphere, orbit, obliquity, and second planetary candidate. **670**, 90 (2023) https://doi.org/10.1051/0004-6361/202244294 arXiv:2211.01474 [astro-ph.EP]

[17] Zechmeister, M., Köhler, J., Chamarthi, S.: Viper: Velocity and IP EstimatoR

[18] Köhler, J., Zechmeister, M., Hatzes, A., Chamarthi, S., Nagel, E., Seemann, U., Ballester, P., Bristow, P., Chaturvedi, P., Dorn, R.J., Guenther, E., Ivanov, V.D., Jung, Y., Kochukhov, O., Marquart, T., Nortmann, L., Palsa, R., Piskunov, N., Reiners, A., Rodler, F., Smoker, J.V.: viper: High-precision radial velocities from the optical to the infrared: Reaching 3 m/s in the K band of CRIRES$^+$ with telluric modelling. **698**, 44 (2025) https://doi.org/10.1051/0004-6361/202553919 arXiv:2505.08315 [astro-ph.IM]

[19] Lomb, N.R.: Least-Squares Frequency Analysis of Unequally Spaced Data. **39**(2), 447–462 (1976) https://doi.org/10.1007/BF00648343

[20] Burt, J.A., Dumusque, X., Halverson, S.: Precise Radial Velocities. arXiv e-prints, 2511–01954 (2025) https://doi.org/10.48550/arXiv.2511.01954 arXiv:2511.01954 [astro-ph.EP]

[21] Anglada-Escudé, G., López-Morales, M., Chambers, J.E.: How Eccentric Orbital Solutions Can Hide Planetary Systems in 2:1 Resonant Orbits. **709**(1), 168–178 (2010) https://doi.org/10.1088/0004-637X/709/1/168 arXiv:0809.1275 [astro-ph]

[22] Wittenmyer, R.A., Clark, J.T., Zhao, J., Horner, J., Wang, S., Johns, D.: Truly eccentric - I. Revisiting eight single-eccentric planetary systems. **484**(4), 5859–5867 (2019) https://doi.org/10.1093/mnras/stz290 arXiv:1901.08471 [astro-ph.EP]

[23] Rein, H., Liu, S.-F.: REBOUND: an open-source multi-purpose N-body code for collisional dynamics. **537**, 128 (2012) https://doi.org/10.1051/0004-6361/201118085 arXiv:1110.4876 [astro-ph.EP]

[24] Rein, H., Tamayo, D.: Second-order variational equations for N-body simulations. **459**(3), 2275–2285 (2016) https://doi.org/10.1093/mnras/stw644 arXiv:1603.03424 [astro-ph.EP]

[25] Su, X.-N., Xie, J.-W., Zhou, J.-L., Thebault, P.: Demographics of exoplanets in binaries. i. architecture of s-type planetary systems revealed by the radial-velocity sample. The Astronomical Journal **162**(6), 272 (2021) https://doi.org/10.3847/1538-3881/ac2ba3

[26] Wang, G., Xuan, J.W., González Picos, D., Zhang, Z., Zhang, Y., Mawet, D., Hsu, C.-C., Wang, J.J., Blake, G.A., Ruffio, J.-B., Horstman, K., Sappey, B., Xin, Y., Finnerty, L., Echeverri, D., Jovanovic, N., Baker, A., Bartos, R., Calvin, B., Cetre, S., Delorme, J.-R., Doppmann, G.W., Fitzgerald, M.P., Liberman, J., López, R.A., Morris, E., Pezzato-Rovner, J., Phillips, C.L., Schofield, T., Skemer, A., Wallace, J.K., Wang, J.: Chemical and Isotopic Homogeneity between the L Dwarf CD-35 2722 B and Its Early M Host Star. **997**(2), 195 (2026) https://doi.org/10.3847/1538-4357/ae232f

[27] Robertson, P., Endl, M., Cochran, W.D., Dodson-Robinson, S.E.: H activity of old m dwarfs: Stellar cycles and mean activity levels for 93 low-mass stars in the solar neighborhood. The Astrophysical Journal **764**(1), 3 (2013) https://doi.org/10.1088/0004-637x/764/1/3

[28] Route, M.: The discovery of solar-like activity cycles beyond the end of the main sequence? The Astrophysical Journal Letters **830**(2), 27 (2016) https://doi.org/10.3847/2041-8205/830/2/l27

[29] Chauvin, G., Lagrange, A.-M., Dumas, C., Zuckerman, B., Mouillet, D., Song, I., Beuzit, J.-L., Lowrance, P.: Giant planet companion to 2masswj1207334-393254. Astronomy amp; Astrophysics **438**(2), 25–28 (2005) https://doi.org/10.1051/0004-6361:200500116

[30] Gauza, B., Béjar, V.J.S., Pérez-Garrido, A., Osorio, M.R.Z., Lodieu, N., Rebolo, R., Pallé, E., Nowak, G.: Discovery of a young planetary mass companion to the nearby m dwarf vhs j125601.92-125723.9. The Astrophysical Journal **804**(2), 96 (2015) https://doi.org/10.1088/0004-637x/804/2/96

[31] Turnbull, M.C.: ExoCat-1: The Nearby Stellar Systems Catalog for Exoplanet Imaging Missions. arXiv e-prints, 1510–01731 (2015) https://doi.org/10.48550/arXiv.1510.01731 arXiv:1510.01731 [astro-ph.SR]

[32] Heller, R., Williams, D., Kipping, D., Limbach, M.A., Turner, E., *et al.*: Formation, habitability, and detection of extrasolar moons. Astrobiology **14**(9), 798–835 (2014) https://doi.org/10.1089/ast.2014.1147

[33] Etangs, A., Lissauer, J.J.: The iau working definition of an exoplanet. New Astronomy Reviews **94**, 101641 (2022) https://doi.org/10.1016/j.newar.2022.

101641

[34] Marley, M.S., Saumon, D., Visscher, C., Lupu, R., Freedman, R., Morley, C., Fortney, J.J., Seay, C., Smith, A.J.R.W., Teal, D.J., Wang, R.: The sonora brown dwarf atmosphere and evolution models. i. model description and application to cloudless atmospheres in rainout chemical equilibrium. The Astrophysical Journal **920**(2), 85 (2021) https://doi.org/10.3847/1538-4357/ac141d

[35] Dieterich, S.B., Simler, A., Henry, T.J., Jao, W.-C.: The solar neighborhood. xlvii. comparing m-dwarf models with hubble space telescope dynamical masses and spectroscopy*. The Astronomical Journal **161**(4), 172 (2021) https://doi.org/10.3847/1538-3881/abd2c2

[36] Figueira, P., Pepe, F., Lovis, C., Mayor, M.: Evaluating the stability of atmospheric lines with harps. Astronomy and Astrophysics **515**, 106 (2010) https://doi.org/10.1051/0004-6361/201014005

[37] Peña R., P.A., Jenkins, J.S.: EMPEROR: I. Exoplanet MCMC parallel tempering for RV orbit retrieval. **704**, 323 (2025) https://doi.org/10.1051/0004-6361/202554336 arXiv:2511.05331 [astro-ph.EP]

[38] Peña R, Pablo A., Jenkins, James S.: Closing the evidence gap: reddemcee, a fast adaptive parallel tempering sampler - next-generation ladder adaptation and evidence estimators for parallel tempering. AA **706**, 323 (2026) https://doi.org/10.1051/0004-6361/202556609

[39] Hou, F., Goodman, J., Hogg, D.W., Weare, J., Schwab, C.: An Affine-invariant Sampler for Exoplanet Fitting and Discovery in Radial Velocity Data. **745**(2), 198 (2012) https://doi.org/10.1088/0004-637X/745/2/198 arXiv:1104.2612 [astro-ph.IM]

[40] Rasmussen, C.E., Williams, C.K.I.: Gaussian Processes for Machine Learning. The MIT Press, ??? (2006)

[41] Foreman-Mackey, D., Agol, E., Angus, R., Ambikasaran, S.: Fast and scalable gaussian process modeling with applications to astronomical time series. ArXiv (2017)

[42] Foreman-Mackey, D.: Scalable Backpropagation for Gaussian Processes using Celerite. Research Notes of the American Astronomical Society **2**(1), 31 (2018) https://doi.org/10.3847/2515-5172/aaaf6c

[43] Rein, H., Spiegel, D.S.: IAS15: a fast, adaptive, high-order integrator for gravitational dynamics, accurate to machine precision over a billion orbits. **446**(2), 1424–1437 (2015) https://doi.org/10.1093/mnras/stu2164 arXiv:1409.4779 [astro-ph.EP]

[44] Gayon, J., Bois, E., Scholl, H.: Dynamics of planets in retrograde mean motion resonance. Celestial Mechanics and Dynamical Astronomy **103**(3), 267–279 (2009) https://doi.org/10.1007/s10569-009-9191-8 arXiv:0902.0428 [astro-ph.EP]

[45] Domingos, R.C., Winter, O.C., Yokoyama, T.: Stable satellites around extrasolar giant planets. **373**(3), 1227–1234 (2006) https://doi.org/10.1111/j.1365-2966.2006.11104.x

[46] Baraffe, I., Homeier, D., Allard, F., Chabrier, G.: New evolutionary models for pre-main sequence and main sequence low-mass stars down to the hydrogen-burning limit. **577**, 42 (2015) https://doi.org/10.1051/0004-6361/201425481 arXiv:1503.04107 [astro-ph.SR]

[47] Latouf, N., Wang, S.X., Cale, B., Plavchan, P.: Characterizing and Mitigating Telluric Absorption in Precise Radial Velocities. II. A Study of an M2-type Star. **164**(5), 212 (2022) https://doi.org/10.3847/1538-3881/ac947b arXiv:2206.05233 [astro-ph.EP]

Author Contributions

K.H. wrote the manuscript, analyzed the data, and obtained the results, A.Z. contributed to the writing of the article, conceived the idea, and led the survey. P.P. ran the `EMPEROR` analysis, J.K. assisted with the `viper` analysis, S.D., R.G., and C.L. worked on the observations and analysis. S.P. contributed target-specific insights and contextualization, F.R. and J.S. provided instrument-specific insights, V.d'O., I.C., and I.G. contributed to the observations execution. All the authors reviewed the article and provided feedback.

Competing Interests

The authors declare no competing interests.

Materials & Correspondence

All correspondence and request for materials can be made to Kevin Hoy (kevin.hoy@mail.udp.cl).

Supplemental Information

A Full RV dataset

BJD	Relative RV (m/s)	RV Error (m/s)
2460230.8690	-63.2	70.8
2460280.8132	-391.8	42.1
2460285.8067	-310.4	58.1
2460300.7913	66.3	60.3
2460312.5617	-27.1	69.1
2460318.7713	123.3	50.9
2460320.6801	88.2	61.8
2460328.5502	59.5	44.2
2460339.6561	143.8	53.5
2460370.5365	110.4	68.0
2460388.6270	58.6	60.8
2460600.7588	-437.0	47.8
2460624.8336	-409.1	47.6
2460647.8354	-19.9	46.3
2460660.7900	138.5	62.7
2460666.7973	154.5	66.5
2460674.7425	169.5	49.3
2460683.6364	61.3	45.6
2460688.6133	225.5	57.0
2460696.6456	63.2	79.1
2461030.7490	171.2	86.3
2461051.5616	108.9	44.3
2461081.5592	-84.4	54.5

Table 2 Barycentric Julian dates, radial velocities, and their correlated errors used in this work.

B Full one-satellite model fit corner plot

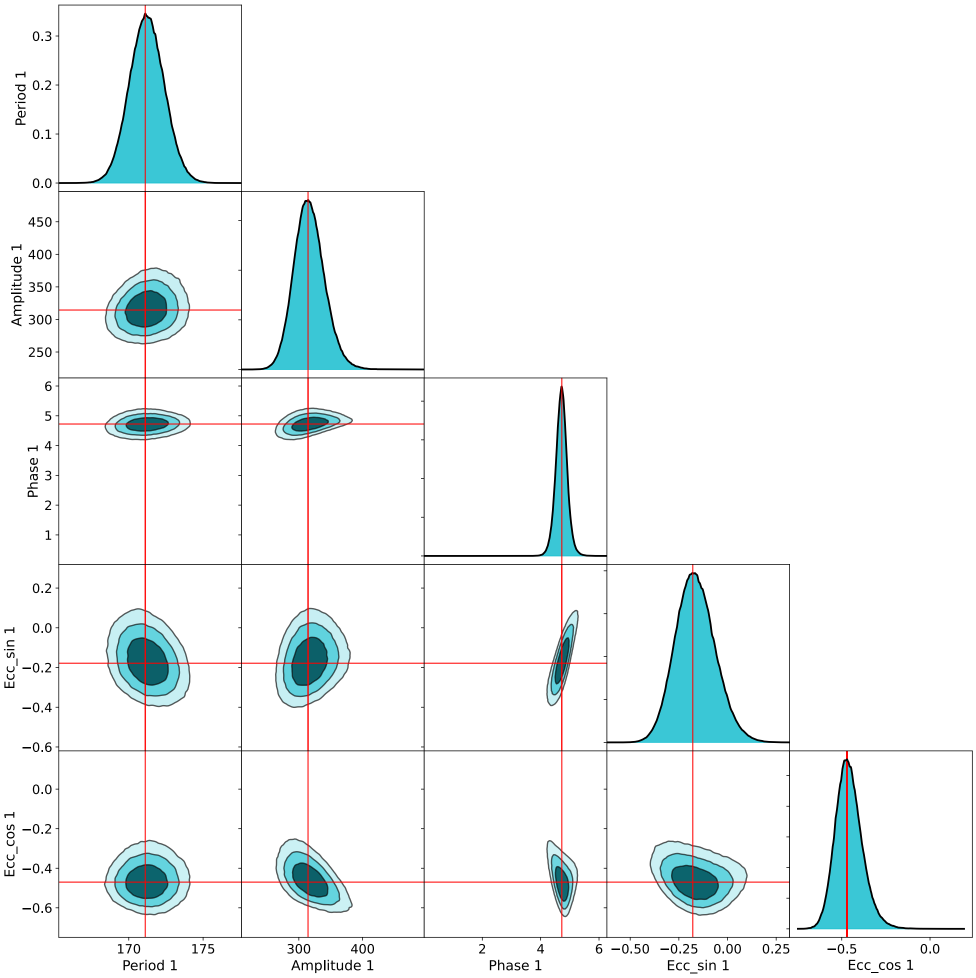

Fig. 13 Corner plot for the derived orbital parameters.

C Phase-folded best-fitting Keplerian models

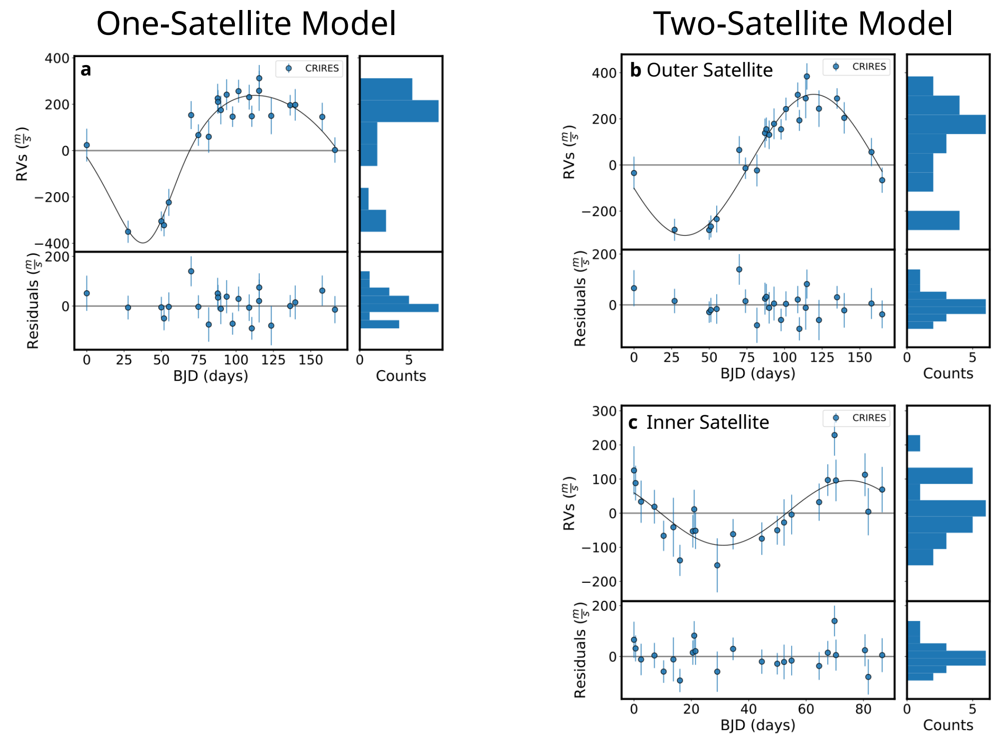

Fig. 14 Best-fitting one-satellite and two-satellite models, phase-folded.

D Projected Model Orbits for Future Observations

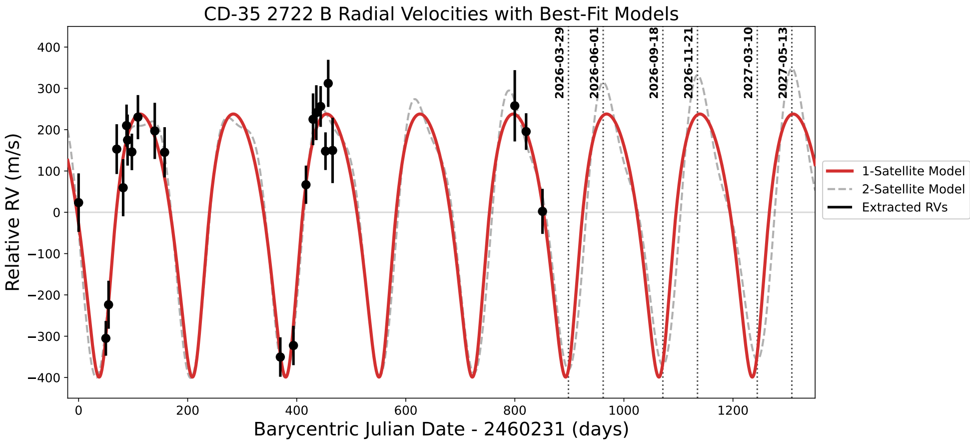

Fig. 15 Best-fitting models projected into the future, to show how they differentiate over time. The strongest differences occur near the maxima and minima, and they grow more disparate over time, due to the orbits not being in exactly 2:1 MMR. The local maxima and minima for the two-satellite model are labelled. While the maxima largely vary in amplitude, the minima more quickly diverge in timing from the one-satellite model.